ChemSusChem

Chemistry Europe
European Chemical Societies Publishing
ChemSusChem

RESEARCH ARTICLE OPEN ACCESS

Electrodeposited MnCo and MnNiCo Spinels for Anion Exchange Membrane Direct Ammonia Fuel Cell Cathodes: An Alternative to Platinum

Mehmet Turan Görüryilmaz[1,2] | Karuppasamy Dharmaraj[1,2] | Iris Dorbandt[1,2] | Erno Kemppainen[1] | Thorsten Schultz[3,4] | Norbert Koch[3,4] | Xuyun Guo[5] | Valeria Nicolosi[5] | Rutger Schlatmann[1] | Michelle P. Browne[3] | Sonya Calnan[1,6]

[1]Institute Competence Centrfe Photovoltaics Berlin, Helmholtz-Zentrum Berlin für Materialien und Energie GmbH, Berlin, Germany | [2]Helmholtz Young Investigator Group Electrocatalysis: Synthesis to Devices, Helmholtz-Zentrum Berlin für Materialien und Energie, Berlin, Germany | [3]Helmholtz-Zentrum Berlin für Materialien und Energie GmbH, Berlin, Germany | [4]Institut für Physik & CSMB, Humboldt-Universität zu Berlin, Berlin, Germany | [5]School of Chemistry, CRANN and AMBER Research Centers, Trinity College Dublin, Dublin, Ireland | [6]Wolfson School of Mechanical, Electrical and Manufacturing Engineering, Loughborough University, Loughborough, Leicestershire, UK

Correspondence: Mehmet Turan Görüryilmaz (mehmet.goerueryilmaz@helmholtz-berlin.de) | Sonya Calnan (s.calnan@lboro.ac.uk)

Received: 30 January 2026 | **Revised:** 20 May 2026 | **Accepted:** 27 May 2026

Keywords: catalyst poisoning | direct ammonia fuel cell | electrochemical impedance spectroscopy | electrodeposition | MnCo spinel | NH_3 crossover | oxygen reduction reaction

ABSTRACT

Direct ammonia fuel cells (DAFCs) hold great promise as clean energy conversion devices due to their carbon-free exhaust, the high energy density and liquid-phase storability of ammonia, and use of an existing production and distribution infrastructure. When using the state-of-the-art anion exchange membranes, ammonia crossover from the cathode to the anode can cause rapid decay in DAFC performance as the current density increases. Mixed-metal oxides containing manganese–nickel–cobalt have emerged as NH_3-tolerant cathode catalysts, but their systematic testing under variable loading conditions in DAFC is rarely reported. Here, we examine low-temperature DAFCs with electrodeposited platinum (Pt), manganese–cobalt oxide ($MnCoO_X$), and manganese–nickel–cobalt oxide ($MnNiCoO_X$) cathodes on Ni foam. To isolate cathodic effects, all cells use identical Pt on Ni Foam anodes with alkaline ammonia feeds. Structural characterization confirms defect-rich spinel coatings. $MnCoO_X$ achieves oxygen reduction reaction performance comparable to Pt, sustaining higher load voltage with lower interfacial resistance and larger capacitance, while $MnNiCoO_X$ shows restricted performance and rapid voltage loss, indicating sluggish charge transfer and fewer active sites. These results identify electrodeposited $MnCoO_X$ on Ni foam as a promising, scalable platinum group metal-free cathode for DAFCs and highlight compositional and mesostructural tuning as key levers to improve catalytic activity and device performance.

1 | Introduction

Mitigating climate change requires shifting away from carbon-heavy energy infrastructure to low-carbon and even carbon-free substitutes. One of the primary causes of global CO_2 emissions is the burning of fossil fuels for transportation, power generation, and industrial uses. Hydrogen has been seen as one potential candidate to serve as the ideal zero-carbon fuel, but drawbacks to its storage, delivery, and safety, most significantly the requirement for cryogenic temperatures or high-pressure vessels, currently preclude its broad introduction to mobile and decentralized uses [1].

Ammonia (NH_3), on the other hand, is one fuel that is free of carbon and provides a singular set of benefits. It is characterized by high volumetric energy density (11.5 MJ/L), is readily liquefiable at 25°C and 10 bar, and is less flammable than hydrogen H_2 and methane, CH_4 [2]. Moreover, the issues of high toxicity and corrosiveness can be managed using mature technologies as evidenced by the well-established global infrastructure for production, storage, and transportation. In comparison to hydrogen, its storage volume and cost are significantly lower, and unlike methanol or hydrocarbon fuels, ammonia does not emit CO_2 during oxidation, emitting mostly water and nitrogen [3–5].

In direct ammonia fuel cells (DAFCs), ammonia is electrochemically oxidized without the precracking into hydrogen needed for conventional fuel cells, making the system architecture less complicated, less energy intensive, and potentially boosting efficiency. Yet, even with all the above benefits, the technology readiness level of DAFCs is relatively low as compared to hydrogen-fed proton-exchange membrane fuel cells and solid oxide fuel cells.

Low-to-intermediate temperature DAFCs typically use an aqueous alkaline electrolyte and an anion exchange membrane (AEM) for charge transport. In alkaline DAFCs, ammonia undergoes electrochemical oxidation at the anode, releasing electrons thereby generating water and nitrogen. The cathode receives oxygen, typically from air or pure O_2, and via the oxygen reduction reaction (ORR), generates hydroxide ions (OH^-). The hydroxide ions migrate from the cathode through the AEM to the anode, donating charge for the ammonia oxidation while the electrons from the anode flow through the external load to complete the electrical circuit. This setup bypasses the need for hydrogen as an intermediate fuel, simplifying logistics.

Despite its advantages, several intrinsic challenges persist in DAFC development. Major limitations in DAFC include low kinetics of the ammonia oxidation reaction (AOR), crossover of ammonia across the membrane, degradation of the catalyst, and relative ease of the solid polymer electrolyte degradation during operation [6, 7]. The AOR requires multistep electron transfer and N—H bond cleavage, leading to high overpotentials, resulting in sluggish AOR kinetics. Another aspect to consider is the ammonia crossover problem, whereby NH_3 readily diffuses across AEMs due to its high solubility in water and molecular diffusivity, causing unwanted oxidation at the cathode and rapid performance degradation through catalyst poisoning and ORR interference [6]. Studies have shown that ammonia permeation rates increase at higher current densities, necessitating careful formulation of membrane materials [8, 9].The relative ease of solid polymer electrolyte degradation used for DAFCs is another issue that needs to be addressed. Alkaline AEMs are prone to degradation in hot, ammonia-rich environments via loss of cationic groups, breakage of polymer chains, among others. This reduces OH^- conductivity and leads to higher Ohmic losses [7]. Like most types of fuel cells, water management and flooding also affect DAFCs. Additionally, both electrodes must balance water generation and removal. Besides, flooding at the cathode can block active sites, while membrane dehydration can limit ion conductivity.

To address these limitations, multiple strategies have emerged. New catalyst designs have been introduced to enhance AOR and ORR kinetics. Most studies seek to enhance AOR performance with PtIr/C catalysts showing significant improvements over Pt/C catalysts. For example, on rotating disk electrodes commercial Pt/C catalysts show limited activity, whereas PtIr/C improves ammonia oxidation activity by over 200%, from 66.3 mA/mg for Pt/C to 216.6 mA/mg [10]. In a DAFC, a PtIr anode achieved an open circuit voltage (OCV) of 0.50 V and peak power density (PPD) of 1.68 mW/cm^2 under ambient conditions [11]. More recent multimetallic catalysts have pushed AOR performance much further. For example, Ni-doped PtMo alloys achieve an AOR onset potential of about 0.49 V versus reversible hydrogen electrode (RHE), peak current densities close to 95 A/g, and DAFC peak power densities of ≈16.7 mW/cm^2 at 40°C [12]. System-level DAFC studies, including passive and stack designs, further show that with optimized AOR catalysts and cell architecture, peak power densities can reach tens of mW/cm^2 per cell under practical conditions [13]. Recent reviews summarize a rapidly expanding landscape of Ir-free and precious-metal-efficient AOR catalysts for low-temperature DAFCs [14]. However, these advances are heavily skewed toward the anode. At the cathode, ORR in ammonia-containing alkaline environments remains relatively sluggish, and conventional Pt-based ORR catalysts are readily poisoned by ammonia and its oxidation intermediates. This makes the development of ammonia-tolerant, preferably platinum group metal (PGM)-free ORR cathodes, a critical yet comparatively underexplored area of research.

Considering the cathode, although the alkaline environment is more favorable than acidic for ORR, there is still scope to improve the reaction kinetics. Additionally, there are operational challenges arising from the operation of the DAFC that affect the performance of the cathode such as gradual degradation of the catalytic activity over time, parasitic reactions caused by NH_3 crossover as well as flooding, among others. Orthogonal tests revealed that cell performance influenced the binder type, binder content, and cathode catalyst loading with the effect reducing in that order, showing the critical influence of morphology and ionomer interaction [15]. A related study optimized the loading at the cathode of the commercial Pt/C catalysts, and the polytetrafluoroethylene (PTFE) hydrophobic layer to control electrode flooding and NH_3 crossover, achieving a power density of 267 mW/cm^2 with 5 cm^2 electrodes [16]. Another group combined a self-developed fluorinated block poly (aryl piperidinium) AEM that maintained high conductivity while minimizing NH_3 crossover, with a Pt/C cathode catalyst mixed with PTFE and achieved a PPD of 525 mW/cm^2 using 5 cm^2 electrodes [17].

Other efforts have focused on the need to replace platinum group catalysts with more abundant elements. Layer engineering of a perovskite cathode catalyst layer ($LaCr_{0.25}Fe_{0.25}Co_{0.5}O_{3-\delta}$/C with tuned carbon/ionomer/PTFE) enabled non-PGM cathodes to rival Pt/C in DAFCs at 80–100°C through improved electronic percolation and mass transport [18]. $LaCr_{0.25}Fe_{0.25}Co_{0.5}O_{3-\delta}$/C achieved an OCV ≈ 0.72 V and ≈320 mA cm^{-2} peak current (air cathode) and maintained ORR in 0.1 M KOH with 0.1 M NH_3, confirming perovskites as ammonia-tolerant cathodes [19]. $MnCoO_X$ spinel catalysts supported on high-surface-area conductive carbon black powder (BP2000) showed better ORR performance in the presence of ammonia than commercial Pt/C, improving tolerance and enhancing peak power output by ≈28% [20]. Another study showed that the optimization of three different binder types (Nafion, PTFE, and Alkymer) with different contents for different

MnCo spinel catalyst loadings in the cathode layer can increase the power density from 120.4 mW/cm^2 to 158.6 mW/cm^2 [15]. Poison-tolerant MnCo spinel cathodes on carbon supports retain ORR activity in the presence of ammonia and can surpass Pt/C in DAFC peak power, positioning MnCo spinels as robust non-PGM cathodes [20]. Bimetallic cobalt spinels (notably $MnCoO_x$ with Mn/Co = 1:2) delivered Pt/C-comparable ORR and retained structure after AST at 80°C in 3.0 M KOH + 3 M NH_3, highlighting the intrinsic ammonia tolerance of MnCo spinel frameworks [21]. Co-doped Ni_4Cu_1 anodes paired with MnCo/C cathodes delivered PPD up to 115.7 mW/cm^2 (on 2.25 cm^2 electrodes) at 80°C (7.0 M NH_3 + 3.0 M KOH), providing a precious-metal-free DAFC benchmark relevant to non-PGM cathode integration [22]. A DAFC cathode-layer optimization study quantified how carbon fraction, PTFE, and ionomer content govern impedance and peak power, offering a transferable framework for MnCo/MnNiCo cathode ink design [18].

Layered perovskite catalysts contain multiple elements, and the optimization of their composition is rather complicated [16]. Additionally, the synthesis of powder catalysts by high-temperature methods over 500°C is relatively energy intensive [18, 20]. Also, current health concerns driving gradual restrictions on the use of per- and polyfluoroalkyl substances (PFAS), including PTFE, might eventually lead to a complete ban in the long run, requiring alternative catalyst configurations. Despite this, most studies on ammonia-tolerant cathode still employ powder catalysts (Pt/C, perovskites, MnCo spinels) sprayed or pressed onto small ($\leq$5 cm^2) carbon-based gas-diffusion layers (GDLs) with PFAS-based binders, whose scalability to larger, binder-free architectures is largely unexplored. Most of the reports in the literature showing relatively high power densities are on relatively small electrode areas, e.g., 1 cm^2 [18, 23], 2.25 cm^2 [21], and 5 cm^2 [16, 17]. Also the corresponding cathode configurations have rarely been benchmarked on larger-area cells where internal resistance, mass transport, and flooding become more critical. Scalable catalyst synthesis methods need to be developed, so that non-PGM cathode concepts demonstrated on $\leq$5 cm^2 cells can be translated to practical electrode areas without loss of performance. Moreover, issues like increased internal resistance of the cell due to larger sized electrodes, uniformity of catalyst application, and mass transport management, among others, are less apparent in relatively small electrode areas, particularly for powder-based cathode layers supported on carbon GDLs. Besides, a detailed understanding of the electrochemical and physicochemical processes governing DAFC operation is essential for improving performance and durability, including separating electrode-specific losses from full cell via simultaneous full cell and cathode-side impedance analysis, clarifying how MnCo and related bimetallic spinels behave when directly integrated on three-dimensional Ni foam current collectors, and resolving whether Ni coincorporation into Mn–Co spinel frameworks enhances or degrades ORR performance under DAFC operating conditions.

Here, we address both scalability and binder-free integration by developing a reproducible route to fabricate $MnCoO_X$ and $MnNiCoO_X$ spinel oxide coated on Ni foam (denoted as MnCo and MnNiCo, respectively) cathodes directly on 25 cm^2 Ni foam using electrodeposition and benchmarking them against a Pt cathode in alkaline AEM-DAFC single cells. We assembled membrane electrode assemblies with identical anodes and membranes to isolate cathodic contributions and employed a test protocol comprising polarization measurements and electrochemical impedance spectroscopy (EIS) to decouple full cell and cathode level losses. To establish coating morphology, crystallinity, and surface states, the electrochemical measurements are complemented with physicochemical characterization consisting of scanning electron microscopy/energy-dispersive X-ray analysis (SEM/EDX) mapping, transmission electron microscopy (TEM), high-resolution TEM (HRTEM), selected area electron diffraction (SAED), high-angle annular dark-field scanning TEM (HAADF–STEM), electron energy loss spectroscopy (EELS) mapping, Raman spectroscopy, and X-ray photoelectron spectroscopy (XPS). Together, this methodology was designed to correlate composition and nanoscale architecture with cathode level behavior and to identify actionable levers for improved non-PGM cathode design in DAFCs.

2 | Results

Morphologies of the freshly prepared MnCo, MnNiCo, and Pt-coated Ni foam samples were investigated using SEM and the elemental composition distributions were determined via EDX mapping. Figure 1a shows the electrodeposited MnCo on Ni foam. The coating has a cracked-soil-like shape. Further magnification shows the porous structure of the electrocatalyst made of thin sheets ranging from 20 to 70 nm in width. Although the coating is not homogeneous, a uniform distribution on the surface of the Ni foam is observed. EDX mapping revealed the elemental composition of the material. Uniform distribution of Mn (purple) and Co (pink) species is shown in the catalyst, as well as the oxidation (red) status. Ni foam was seen as green in the cracks, and no Ni signal was detected within the catalyst layer by EDX. Figure 1b reveals the electrodeposited MnNiCo on Ni foam, and when compared to the MnCo sample, MnNiCo sample shows bigger clusters, while still maintaining the cracked-soil-like structure, although with less defined cluster edges. The thickness of the nanosheets that create the coating ranges between 50– and 100 nm. A uniform distribution can be observed on the Ni foam. EDX mapping shows the Mn (purple), Co (pink), and their oxidizations (red) clearly. Ni (green) can be observed among the cracks, as well as on the catalyst itself, although faint. While it is difficult to determine the loading of porous mixed-metal oxide coatings deposited by electrodeposition, based on the SEM images, we estimate a thickness of ca. 1 µm for MnCo and ca. 2 µm for MnNiCo. Postmortem SEM and EDX show the preservation of the cracked-soil-like structure in a larger area (Figure S1). Elemental mapping reveals no obvious redistribution of Mn, Co, and Ni and no new compositional inhomogeneities between pre- and postmortem electrodes, indicating no detectable structural or compositional degradation.

The TEM images in Figure 2 show nanomorphology and the crystalline structure of the freshly prepared material. The high magnification reveals the crystallinity through the fringes and the low magnification shows the agglomerated particles on Ni foam. SAED confirms the polycrystalline structure of the materials. The continuous rings indicate randomly oriented grains. The identical ring sets for both samples indicate that Mn (and Ni in MnNiCo) are incorporated within a spinel-type oxide framework without an observable change in symmetry within the resolution

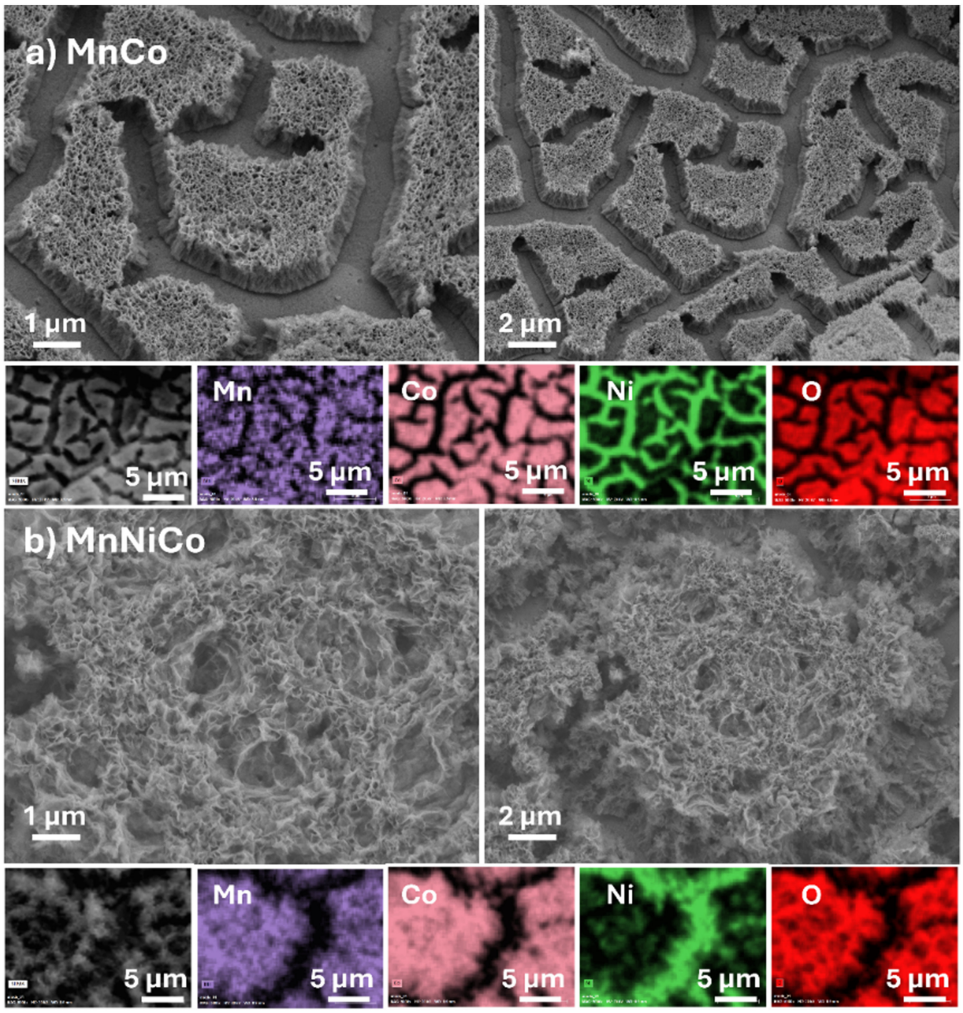

FIGURE 1 | SEM and EDX mapping images of freshly prepared (a) MnCo on Ni foam and (b) MnNiCo on Ni foam.

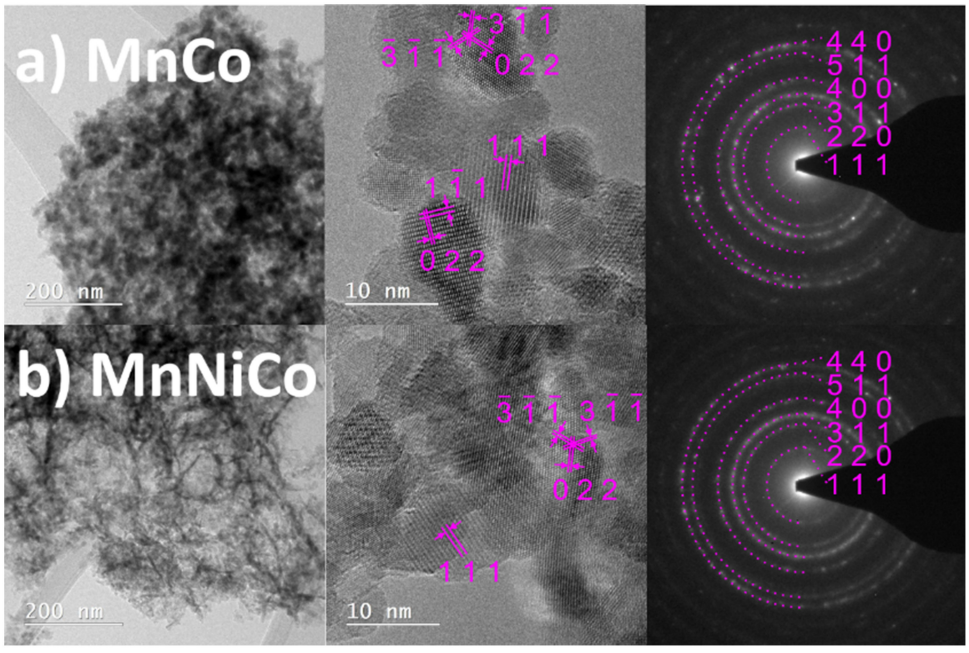

FIGURE 2 | TEM and HRTEM images and SAED patterns of (a) MnCo on Ni foam, (b) MnNiCo on Ni foam.

of SAED. The measured rings correspond to the (111), (220), (311), (400), (511), and (440) families, confirming a polycrystalline spinel-type structure (space group Fd-3m), with (311) having the highest intensity (ICDD #42–1467). Figure S2 shows the elemental mapping of the electrocatalysts. While the Co and Mn distributions are uniform for both samples, the Ni distribution for the MnNiCo sample is not completely uniform. The mapping also shows that the Mn and Co concentrations are reduced with the addition of Ni for MnNiCo sample compared to MnCo sample.

XPS measurements were also conducted on freshly prepared samples to analyze the oxidation states of the Mn, Ni, and Co species and to determine their elemental contributions, Figure 3. Due to the higher surface sensitivity and higher chemical resolution of XPS compared to EDX, nickel species are detected both for the MnCo and MnNiCo samples. Moreover, based on the EDX elemental maps shown in Figure 1b, distinguishing between Ni foam and catalyst contributions is not possible. The Ni 2p core level indicates Ni^{2+} oxidation states, most likely reflecting a mixture of NiO- and $Ni(OH)_2$ [24].

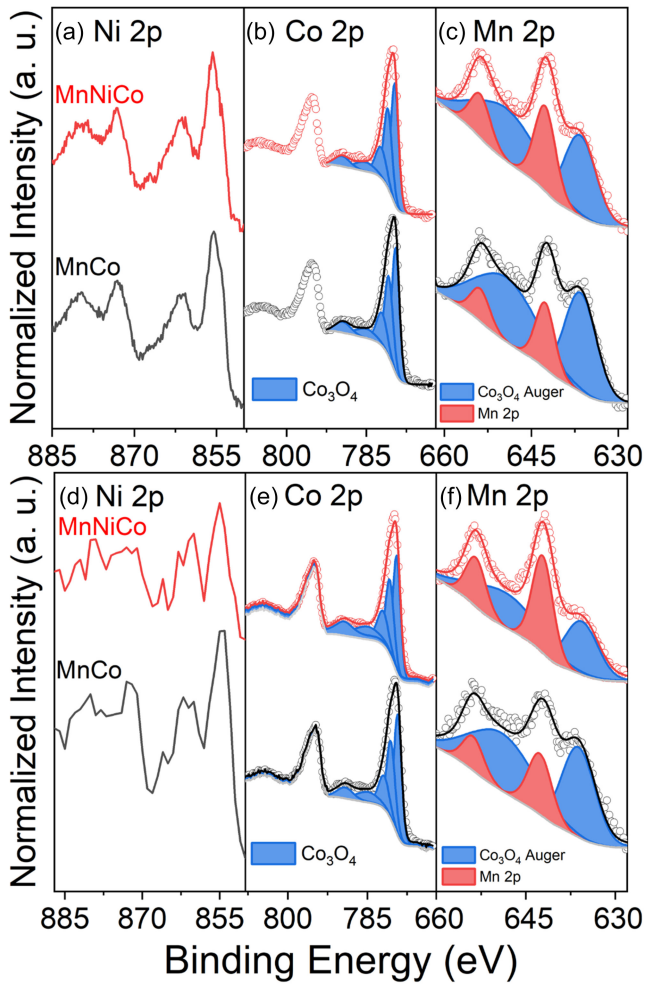

FIGURE 3 | Premortem (a) Ni 2p, (b) Co 2p, and (c) Mn 2p and postmortem (d) Ni 2p, (e) Co 2p, and (f) Mn 2p core levels of freshly prepared MnCo (bottom) and MnNiCo (top) samples. Some Co LMM Auger peaks overlap with the Mn 2p peaks in (c) and (f). In (a) and (d), the lines represent the experimental data while in others the circles represent the experimental data, and the lines represent the models.

The Co 2p core-level regions for the MnCo and MnNiCo samples were fitted with contributions of Co_3O_4 adapted from Biesinger et al. [25]. No significant differences in the Co 2p core levels were observed between the two samples.

The Mn 2p core level for the MnCo and MnNiCo samples, shown in Figure 3c, overlapped with Co LMM Auger peaks. A Co LMM Auger spectrum of a reference sample without Mn is shown in Figure S3, and these peaks were constrained accordingly. Binding energies of Mn^{2+}, Mn^{3+}, and Mn^{4+} are very similar, making reliable oxidation state assignments possible only through detailed peak fitting with high-quality data [26, 27]. This approach was not feasible here due to the low manganese content and overlap with Co LMM peaks. Nevertheless, the overlap enables a direct comparison of elemental contributions from cobalt and manganese. Use of the O 1s spectra to distinguish between Co and Mn is not possible as we cannot rule out contributions from potential oxidation of the Ni foam.

Postmortem XPS measurements were conducted on both samples after DAFC operation to assess surface chemical changes (Figure 3d–f). The Ni 2p core level retains its Ni^{2+} character in both samples, consistent with a surface mixture of NiO- and $Ni(OH)_2$-like species, as observed premortem. Substrate and catalyst Ni contributions remain indistinguishable, as before. A slight downward shift in the Ni $2p_{3/2}$ binding energy is observed for MnCo postmortem (≈854.0 eV vs. ≈855.5 eV), which may reflect partial dehydroxylation of the Ni foam surface under cathodic polarization. The MnNiCo sample shows a smaller shift and a comparatively higher overall Ni signal, consistent with the greater Ni content of that catalyst and corroborating the near-surface Ni enrichment identified by AEY-XAS.

The Co 2p core levels show no significant changes in peak position, spin-orbit splitting, or satellite structure between pre- and postmortem states for either sample, indicating retention of the Co_3O_4-like spinel environment through DAFC operation. The Mn 2p core levels similarly show no substantial shift in binding energy postmortem, and the Co LMM Auger overlap discussed for the premortem spectra applies equally here, precluding reliable oxidation state assignment. The overall spectral stability of both Co 2p and Mn 2p confirms that the spinel framework is chemically preserved after operation.

Raman spectroscopy was used to investigate the structural nature of the freshly prepared electrocatalysts (Figure 4). For MnCo, all the observed peaks at 190 cm^{-1} (F_2g) 483 cm^{-1} (Eg), 529 cm^{-1} and 618 cm^{-1} (both F_2g) as well as the 686 cm^{-1} peak attributed to the A_{1g} symmetry of octahedrally coordinated Co are associated with the Co_3O_4 spinel [28]. The same spinel peaks occur at 194 cm^{-1}, 485 cm^{-1}, 527 cm^{-1}, 618 cm^{-1}, and 691 cm^{-1}, respectively, for the MnNiCo sample. The Raman peak positions in both samples exhibit small shifts which signify the defective structure of the electrocatalyst compared to the pure cobalt spinel [28, 29]. Mn peaks are known to be difficult to observe because of the overlapping of different phases and the sensitivity of the samples to the equipped laser [30]. A small shoulder, possibly an emerging peak, at 651 cm^{-1} for MnNiCo sample was observed for A_{1g} mode consistent with the Mn–O breathing vibration of divalent Mn ions in tetrahedral coordination [31]. Same peak was observed at 653 cm^{-1} for MnCo coated Ni foam. Shifts of the A_{1g} symmetry

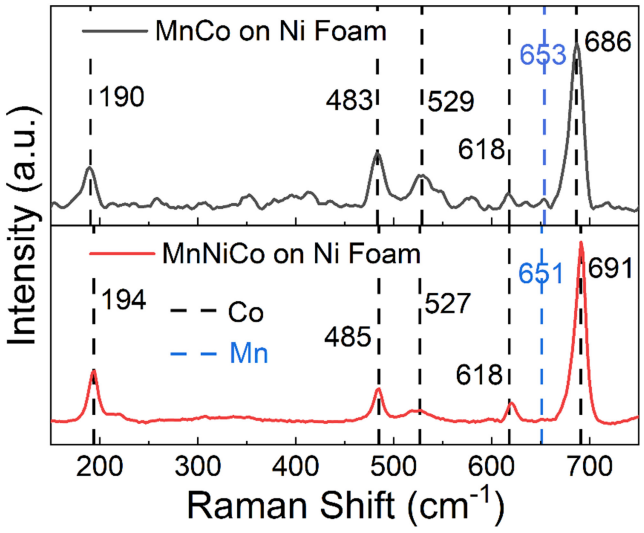

FIGURE 4 | Raman spectra of freshly electrodeposited MnCo and MnNiCo samples on Ni Foam.

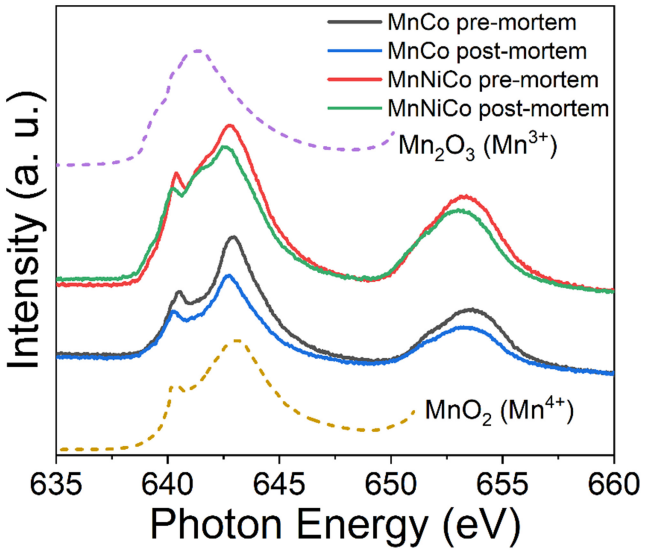

FIGURE 5 | Mn L-edge XAS spectra collected in total electron yield mode for MnCo and MnNiCo on Ni foam, before (premortem) and after (postmortem) DAFC operation. MnCo shows good agreement with MnO_2 (Mn^{4+}) in both states. MnNiCo exhibits an additional shoulder between 641 and 642 eV indicative of Mn^{3+}, reflecting a more reduced Mn species relative to MnCo.

peak toward lower wavenumbers indicate increased substitution of Co by foreign atoms at octahedral sites in the spinel [28]. Ni addition modifies the spinel lattice, as seen by the A_1g position close to that of Co_3O_4 for MnNiCo sample, but Figure S2 shows segregation of Ni that dilutes the Co–Mn content at the surface. This dilution and segregation likely outweigh any local structural regularization around Co, leading to poorer ORR performance in the DAFC.

Because the Mn signal in XPS was too weak for reliable analysis, additional XAS measurements were performed at the ENERGIZE beamline at BESSY II, where the technique is more sensitive to low Mn concentrations. The Ni and Co XAS spectra showed no significant differences between MnCo and MnNiCo, nor between pristine and postmortem samples (Figure S4). This is consistent with Co 2p XPS spectra (Figure 3). Although the Mn 2p XPS spectra did not allow a meaningful analysis of the Mn chemical state, the Mn L-edge XAS spectra shown in Figure 5 provide clearer insight into the Mn oxidation state. Comparison with reference spectra [32] shows that the MnCo samples are in good agreement with MnO_2 (Mn^{4+}), both before and after reaction. In contrast, the MnNiCo samples exhibit an additional shoulder between 641 and 642 eV in both the pristine and postmortem state, indicating the presence of Mn^{3+} and thus a more reduced Mn species compared with the MnCo samples. The increased Mn signal may reflect either a higher near-surface Mn contribution (e.g., relative Mn enrichment due to subtle cation redistribution) and/or a shift toward more oxidized Mn species, both of which can increase L-edge absorption intensity; however, these possibilities cannot be separated unambiguously from intensity trends alone. The Co L-edge spectra are broadly stable between the pre- and the postmortem conditions for MnCo sample and consistent with the Raman and XPS for Co_3O_4-like environment. At the Ni L-edge, the bare Ni foam reference shows the expected Ni^{2+}-dominated lineshape, characteristic of surface oxidation. For MnCo sample, the pre- and postmortem Ni L-edge spectra remain similar in intensity and shape, consistent with Ni originating primarily from the Ni foam substrate and indicating no clear evidence for strong postoperation Ni enrichment at the surface. By contrast, MnNiCo shows noticeably elevated postmortem Ni L-edge intensity (particularly around the Ni L_3 feature) compared to its premortem spectrum, suggesting increased Ni surface segregation/exposure during operation. This trend is consistent with the EELS and XPS observations that Ni is not uniformly distributed in MnNiCo and that Ni-rich surface domains can dilute or mask the catalytically relevant Co–Mn spinel environment, providing a plausible surface chemistry rationale for the lower DAFC performance of MnNiCo relative to MnCo.

The MnCo and MnNiCo catalysts were investigated for the ORR in DAFCs (Figure 6). From Figure 6a, the MnCo-based cell delivers the highest peak power and current density, surpassing even the Pt cathode, while MnNiCo cell shows poor current performance despite a relatively high cell OCV (0.62 V). This drop in voltage at early current onset (to ≈0.44 V at 5 mA) reflects poor kinetics. MnCo catalyst combines a relatively high OCV (0.47 V) with sustained voltage under load, indicating better kinetic accessibility of ORR sites and stability. This matches prior findings that Mn–Co oxide mixtures can display enhanced ORR activity due to improved oxygen intermediate binding and synergistic electronic interactions [33].

The cathodic curves, Figure 6b, confirm MnCo cathode's superior voltage retention under increasing current. MnNiCo cathode's high open-circuit potential (OCP, 1.06 V vs. RHE) is again contrasted by a steep performance loss. The literature suggests that while ternary MnNiCo oxides may form high-surface-area structures, they can suffer from sluggish oxygen reduction kinetics due to competitive adsorption phenomena or phase segregation [34].

From Figure 6c, the EIS results further support the performance trends observed in the polarization curves. At 0.2 V, the full cell impedance spectra show that the MnNiCo-based cell exhibits

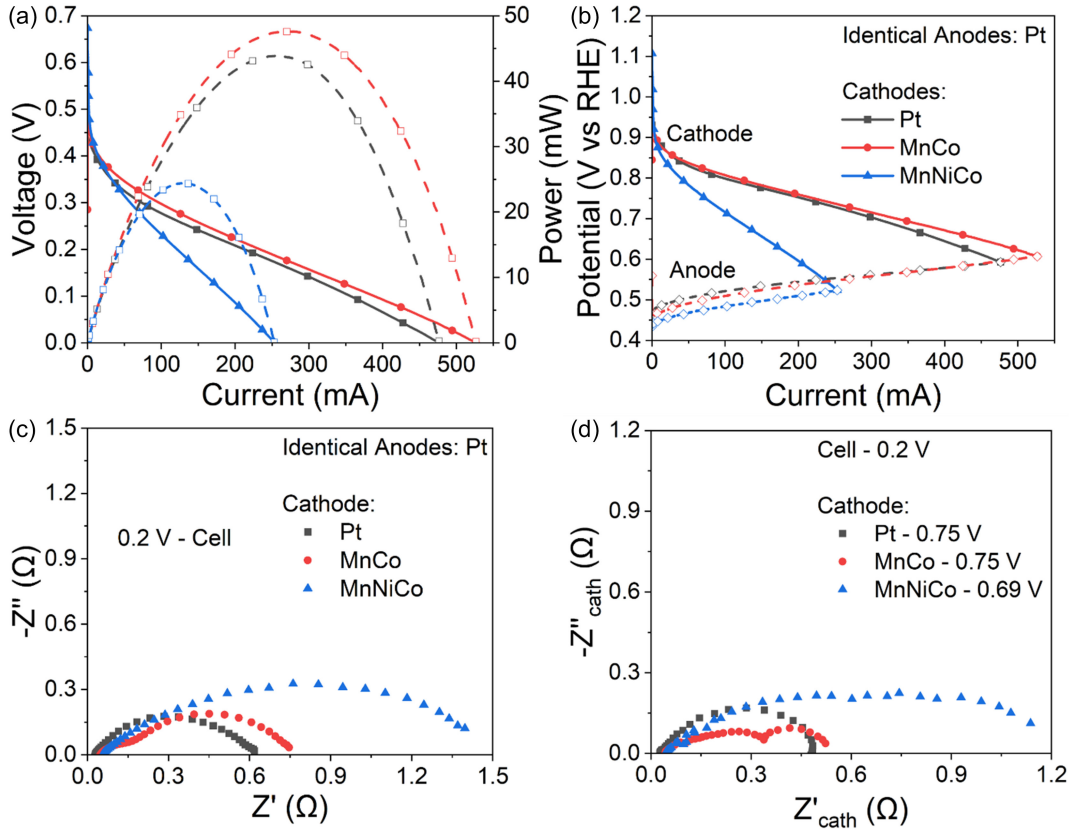

FIGURE 6 | (a) Polarization curves of the cells, (b) the corresponding potentials at the cathode and anode, (c) PEIS values of the full cell, operating at 0.2 V, (d) PEIS values of the cathode while the full cell operates at 0.2 V. The DAFC was composed of a FAA-3-PK-130 (Fumasep) AEM and ≈0.65 C/cm^2 Pt loading on 25 cm^2 nickel foam for anode, ≈0.65 C/cm^2 Pt or MnCo or MnNiCo loading on 25 cm^2 nickel foam for cathode. The cell temperature was fixed to 60°C. Cathode flow rate was 50 sccm O_2 at 1 bar and anode flow rate was 25 mL/min of a mixture of 1.0 M KOH and 1.0 M NH_3.

the largest semicircle, indicating the highest overall polarization resistance R_p among the three cathode configurations. The Pt-based cell displays a total R_p of about 0.58 Ω, characteristic of fast kinetics and low interfacial resistance. The MnCo-based cell presents two distinguishable semicircles, a smaller high-frequency semicircle (≈0.10 Ω), associated with charge transfer processes, and a larger low-frequency arc (≈0.59 Ω), associated with slower transport or interfacial phenomena. Thus, the MnCo cell has a lower high-frequency (charge transfer) resistance than Pt, but a higher overall polarization resistance due to the additional low-frequency limitation.

Considering the EIS of individual electrodes from the plots Figure 6d and from Figure S5, the Pt cathode shows a moderate charge transfer resistance and intermediate double-layer capacitance, corresponding to a single arc/peak. In contrast, the MnCo cathode again exhibits two well-defined semicircles and the highest double-layer capacitance, suggesting a more extended and heterogeneous electrochemical interface. Comparing the SEM images (Figure 1 for MnCo and Figure S6 for Pt), MnCo and MnNiCo exhibit a more complete substrate coverage and likely thicker catalyst layer. Matching the electrode performance at the EIS measurement potential (Figure 6b), the total resistances of Pt and MnCo are roughly equal to each other. The matching peak frequencies of the high-frequency arc indicate that ORR proceeds at roughly the same rate at the active sites of both catalysts, and the porous structure of MnCo giving it a higher surface area than Pt is important for its better performance at higher current densities. The MnCo performance is, however, likely limited by additional mass transport losses, exhibited as the additional low-frequency arc, which is another aspect of the more complete surface coverage and thicker catalyst layer of MnCo compared to Pt. Therefore, as the low-frequency arc corresponds to about 40% of the MnCo cathode resistance, further optimization of MnCo deposition for reduced mass-transport losses could improve its performance significantly. Notably, MnCo's larger double-layer capacitance may arise from increased surface roughness and defect sites, enhancing charge storage and surface adsorption. This is consistent with findings from hybrid Mn–Co oxide catalysts showing enhanced ORR performance and durability in alkaline conditions After 3 h of conditioning and during 3 h testing, the MnCo cathode provided the best performance result and surpassed Pt in peak power and sustained voltage (Figure S7).

These results reinforce that MnCo offers a balance of favorable interfacial properties and sufficient catalytic activity, which contributes to its competitive DAFC performance relative to Pt. The superior performance of the MnCo cathode can be attributed to several synergistic factors. The bimetallic composition provides catalytic complementarity. Cobalt is known to facilitate O—O bond cleavage, while manganese modulates the surface oxygen binding energy, collectively promoting a near four-electron ORR pathway [34]. XPS and TEM mapping suggest that Ni addition dilutes the surface Co–Mn spinel and introduces

Ni^{2+}-rich domains ($NiO/Ni(OH)_2$-like), which are largely inactive for ORR. Since octahedral Co^{3+} in Co_3O_4 is generally regarded as the main active site [35], this dilution and partial replacement by Ni^{2+} likely contributes to the lower DAFC performance of MnNiCo compared to MnCo. Electrochemical impedance analysis further reveals a higher double-layer capacitance for MnCo compared to Pt, suggesting enhanced capacitive buffering at the electrode–electrolyte interface. This may allow for more effective tolerance of intermediate poisoning species and thus contribute to improved stability during sustained operation. Although some diffusion-related limitations are apparent in the impedance spectra, they are evidently outweighed by the kinetic benefits afforded by the MnCo composition. In contrast, the MnNiCo cathode, despite its initially high OCP, displays poor current output under load. This discrepancy may arise from competing redox processes, suboptimal electrical conductivity, or structural instability under DAFC operating conditions, potentially leading to partial catalyst deactivation or diminished active site availability during operation.

3 | Discussion

To date, polymeric electrolyte membranes that are impervious to NH_3 are not readily available. This work was aimed at studying nonplatinum group ORR electrocatalysts for DAFCs aimed at replacing precious metals while minimizing catalyst poisoning via unavoidable crossover of NH_3 from the anode. To achieve this aim, we developed a reproducible route to fabricate MnCo and MnNiCo spinel oxide cathodes directly on 25 cm^2 Ni foam using electrodeposition and benchmarking them against a Pt cathode in alkaline AEM-DAFC single cells. This approach omitted binder materials and addition of PFSAs, whose use, is likely to be restricted for environment and sustainability concerns. Comprehensive characterization (SEM/EDX, TEM/SAED, Raman, XPS) showed that MnCo and MnNiCo coatings form defect-rich, polycrystalline spinels with nanosheet "cracked-soil" morphologies that maximize interfacial area while maintaining electronic connectivity through the Ni scaffold. While surface spectroscopy confirmed Co in Co_3O_4-like environments and Ni predominantly as Ni^{2+} species, the Mn oxidation state could not be unambiguously resolved due to overlap with Co Auger features, motivating operando, element-specific probes in future studies. Electrochemically, the MnCo cathode delivered the most favorable polarization response among the oxides and, under the conditions tested, surpassed Pt in peak power and sustained voltage. Impedance analysis was consistent with a balanced interface. Relatively low high-frequency charge transfer resistance combined with a large effective interfacial capacitance is consistent with high roughness and abundant adsorption sites, leading to robust oxygen reduction kinetics even in ammonia-containing alkaline electrolyte. In contrast, MnNiCo, despite a deceptively high OCV, exhibited rapid voltage losses and, from EIS, a slightly higher series resistance together with markedly larger charge transfer and low-frequency resistances, indicating slower ORR kinetics compounded by transport/adsorption limitations. The performance gap is plausibly rooted in site chemistry (dilution of catalytically active Co–Mn spinel by largely ORR-inactive Ni^{2+} domains).

All binder-free electrodes showed sufficient operational stability over the multihour conditioning and diagnostic protocol (3 h of conditioning followed by 3 h of performance testing) under different load conditions, which is not usually reported for DAFCs. Posttest structural characterization (SEM, EDX, XAS, and XPS) was performed. Using reference electrodes, we decoupled full cell and cathode level losses arising from using the different ORR catalysts proving the superior performance of MnCo compared to Pt, in agreement with the literature [19, 20]. The main limitation of our study was the relatively low performance of the DAFCs which may be attributed to relatively low durability of the membrane used, which prevented operation at temperatures exceeding 60°C at which high performance is usually reported [19, 20, 36] and the suboptimal mass transport and/or water management which were not specifically optimized for scaling. Nevertheless, these results demonstrate that directly electrodeposited spinel-type oxides on Ni foam can serve as a low-cost, effective binder-free PGM-free cathodes that remain stable over the time window required for controlled performance benchmarking and impedance diagnostics for scaling DAFCs operated in alkaline media. A comparison of studies is shown in Table S3 [5, 15, 18–20, 22, 37].

4 | Conclusions

NH_3 crossover across polymeric membranes causes the performance of DAFCs to fade at an unacceptably high rate via poisoning of the ORR catalyst. We have shown that electrodeposited MnCo spinels are relatively tolerant of NH_3 poisoning and thus capable of outperforming Pt as ORR catalysts. Further, the operational stability of these catalysts enables comprehensive characterization of DAFC behavior under the applied loading protocol over several hours. Consistent with this performance, AEY-mode XAS shows largely preserved Mn/Co L-edge lineshapes for MnCo after DAFC operation, whereas MnNiCo exhibits an increased postmortem Ni L-edge contribution indicative of near-surface Ni segregation/exposure that can dilute Co–Mn ORR-active sites. Collectively, these results establish electrodeposited MnCo spinels as promising PGM-free DAFC cathodes that combine scalable fabrication with competitive activity and interfacial properties suited to alkaline, ammonia-rich environments. They also define clear levers for further improvement: preserving Co^{3+}-rich octahedral networks via controlled cation ratios (avoiding Ni-induced dilution and Ni-rich domains), constraining nanosheet thickness to tens of nanometers while maintaining open porosity; and tuning defect density to balance adsorption capacity with intrinsic turnover. Future work should couple operando spectroscopy (XANES/EXAFS or soft XAS/Raman) with impedance/transport diagnostics to resolve active-site valence under bias and pursue extended durability and stress testing under realistic DAFC operation to quantify long-term degradation mechanisms. With targeted compositional and architectural optimization, MnCo-based cathodes can provide a practical path toward efficient, robust, and cost-effective DAFC systems. Moreover, such a durable ORR catalyst synthesized via simple electrodeposition at low temperatures can serve as a relatively low-cost platform for screening and optimizing the AOR catalyst, water management strategies, and membrane durability.

Acknowledgments

This research was mainly done under the TELEGRAM project which received funding from the European Union's Horizon 2020 Research and Innovation programme under grant agreement No. 101006941. The authors also acknowledge support from the German Federal Ministry of Research, Technology and Space in the framework of the project CatLab (03EW0015A/B). We gratefully acknowledge the Helmholtz Association's Initiative and Networking Fund (Helmholtz Young Investigator Group VH-NG-1719). The authors wish to thank the support of the Research Ireland-funded AMBER Research Centre and the Research Ireland Frontiers for the Future award (grant nos. 12/RC/2278_P2 and 20/FFP-A/8950, respectively). Furthermore, we thank the Advanced Microscopy Laboratory in CRANN for the provision of their facilities and thank Clive Downing for assisting in the nonroutine maintenance of the microscope.

Open Access funding enabled and organized by Projekt DEAL.

Funding

This work was supported by the Horizon 2020 Framework Programme (101006941), CatLab (03EW0015A/B), Research Ireland (12/RC/2278_P2, 20/FFP-A/8950), and Helmholtz Young Investigator Group (VH-NG-1719).

Conflicts of Interest

The authors declare no conflicts of interest.

References

1. G. Jeerh, M. Zhang, and S. Tao, "Recent Progress in Ammonia Fuel Cells and Their Potential Applications," *Journal of Materials Chemistry A* 9, no. 2 (2021): 727–752, https://doi.org/10.1039/d0ta08810b.

2. U. J. Pfahl, M. C. Ross, J. E. Shepherd, K. O. Pasamehmetoglu, and C. Unal, "Flammability Limits, Ignition Energy, and Flame Speeds in H_2-CH_4-NH_3- N_2O-O_2-N_2 Mixtures," *Combustion and Flame* 123, no. 1–2 (2000): 140–158, https://doi.org/10.1016/S0010-2180(00)00152-8.

3. H. Shi, J. Tang, W. Yu, M. O. Tadé, and Z. Shao, "Advances in Power Generation From Ammonia via Electrocatalytic Oxidation in Direct Ammonia Fuel Cells," *Chemical Engineering Journal* 488 (2024): 150896, https://doi.org/10.1016/j.cej.2024.150896.

4. D. K. Bora and A. Faik, "Direct Ammonia Fuel Cells for Power Generation: Recent Technological Advances and Mobility Applications," *Current Opinion in Green and Sustainable Chemistry* 48 (2024): 100944, https://doi.org/10.1016/j.cogsc.2024.100944.

5. T. Wang, Y. Zhao, B. P. Setzler, and Y. Yan, "Improving Performance and Durability of Low Temperature Direct Ammonia Fuel Cells: Effect of Backpressure and Oxygen Reduction Catalysts," *Journal of the Electrochemical Society* 168, no. 1 (2021): 014507, https://doi.org/10.1149/1945-7111/abdcca.

6. D. R. Dekel, K. Yassin, I. G. Rasin, and S. Brandon, "Modeling Direct Ammonia Anion-Exchange Membrane Fuel Cells," *Journal of Power Sources* 558 (2023): 232616, https://doi.org/10.1016/j.jpowsour.2022.232616.

7. Y. Liu, Z. Pan, O. C. Esan, X. Xu, and L. An, "Performance Characteristics of a Direct Ammonia Fuel Cell With an Anion Exchange Membrane," *Energy & Fuels* 36, no. 21 (2022): 13203–13211, https://doi.org/10.1021/acs.energyfuels.2c02951.

8. F. Dong, Z. Hu, Z. Wang, et al., "Modeling and Optimizing Anode Catalyst Layer for Direct Ammonia Fuel Cell," *Energy Nexus* 9 (2023), https://doi.org/10.1016/j.nexus.2022.100170.

9. M. T. Görüryilmaz, E. Kemppainen, I. Dorbandt, et al., "*Test Procedures for the Evaluation of the Performance and Stability of Direct Ammonia Fuel Cells*," preprint, *ChemRxiv*, (2025), https://chemrxiv.org/doi/full/10.26434/chemrxiv-2025-wm493.

10. Z. Wang, Q. Xiao, and Z. Hu, "Efficient Anode PtIr Catalysts for Anion Exchange Membrane Direct Ammonia Fuel Cells," *Eighth International Conference on Energy Materials and Electrical Engineering (ICEMEE 2022)* 12598 (2023): 110, https://doi.org/10.1117/12.2673086.

11. R. Chen, S. Zheng, Y. Yao, et al., "Performance of Direct Ammonia Fuel Cell With PtIr/C, PtRu/C, and Pt/C as Anode Electrocatalysts Under Mild Conditions," *International Journal of Hydrogen Energy* 46, no. 54 (2021): 27749–27757, https://doi.org/10.1016/j.ijhydene.2021.06.001.

12. S. Liu, Y. Jiang, M. Wang, et al., "Awakening (220) as One More Active Facet of PtMo Alloy via Single-Atom Doping to Boost Ammonia Electrooxidation in Direct Ammonia Fuel Cell," *Advanced Functional Materials* 33, no. 47 (2023): 2306204, https://doi.org/10.1002/adfm.202306204.

13. Y. Liu, Z. Pan, O. C. Esan, X. Huo, X. Shi, and L. An, "Development and Performance Evaluation of a Passive Direct Ammonia Fuel Cell," *Journal of Power Sources* 570 (2023): 233057, https://doi.org/10.1016/j.jpowsour.2023.233057.

14. H. Y. Kim, J. Kim, E. Lee, et al., "Electrocatalyst Design Strategies Towards High Performance Anion-Exchange Membrane-Based Direct Ammonia Fuel Cells," *Journal of Materials Chemistry A* 13, no. 9 (2025): 6176–6204, https://doi.org/10.1039/d4ta07723g.

15. Z. Hu, D. Yang, C. Zhang, P. Ming, and Q. Xiao, "Optimization of the Cathode Catalyst Layer for Boosting Direct Ammonia Fuel Cell Performance by Orthogonal Tests," *Energy & Fuels* 37, no. 12 (2023): 8600–8613, https://doi.org/10.1021/acs.energyfuels.3c01039.

16. D. Kim, J. Son, Y. Lee, Y. Shin, S. M. Kim, and S. Jang, "Boosting Direct-Ammonia Fuel Cell Performance via Cathode Configuration Optimization," *International Journal of Hydrogen Energy* 101 (2025): 1496–1502, https://doi.org/10.1016/j.ijhydene.2025.01.007.

17. Y. Han, Y. Zhao, Z. Ren, et al., "Fluorinated Block Poly (Aryl Piperidinium) Anion Exchange Membranes Enabling High-Performance Low-Temperature Direct Ammonia Fuel Cell," *Journal of Membrane Science* 733 (2025): 124332, https://doi.org/10.1016/j.memsci.2025.124332.

18. G. Jeerh, P. Zou, M. Zhang, and S. Tao, "Optimization of a Perovskite Oxide-Based Cathode Catalyst Layer on Performance of Direct Ammonia Fuel Cells," *ACS Applied Materials & Interfaces* 15, no. 1 (2023): 1029–1041, https://doi.org/10.1021/acsami.2c17253.

19. G. Jeerh, P. Zou, M. Zhang, and S. Tao, "Perovskite Oxide LaCr0.25Fe0.25Co0.5O3-δ as an Efficient Non-Noble Cathode for Direct Ammonia Fuel Cells," *Applied Catalysis B: Environmental* 319 (2022): 121919, https://doi.org/10.1016/j.apcatb.2022.121919.

20. Z. Hu, Q. Xiao, D. Xiao, et al., "Synthesis of Anti-Poisoning Spinel Mn-Co-C as Cathode Catalysts for Low-Temperature Anion Exchange Membrane Direct Ammonia Fuel Cells," *ACS Applied Materials & Interfaces* 13, no. 45 (2021): 53945–53954, https://doi.org/10.1021/acsami.1c16251.

21. K. Dharmaraj, R. Hanna, F. Ruske, et al., "Ammonia Tolerant Alkaline Oxygen Reduction Reaction on Bimetallic Cobalt Spinels," *Chemical Engineering Journal* 522 (2025): 167192, https://doi.org/10.1016/j.cej.2025.167192.

22. Z. Hu, S. Lu, F. Tang, et al., "High-Performance Precious Metal-Free Direct Ammonia Fuel Cells Endowed by Co-Doped Ni_4Cu_1 Anode Catalysts," *Applied Catalysis B: Environmental* 334 (2023): 122856, https://doi.org/10.1016/j.apcatb.2023.122856.

23. W. Li, Y. LIU, Z. Pan, and Y. LIU, "A Hybrid Direct Ammonia Fuel Cell," *ECS Meeting Abstracts* MA2023-02, no. 1 (2023): 61–61, https://doi.org/10.1149/ma2023-02161mtgabs.

24. M. C. Biesinger, L. W. M. Lau, A. R. Gerson, and R. S. C. Smart, "The Role of the Auger Parameter in XPS Studies of Nickel Metal, Halides and Oxides," *Physical Chemistry Chemical Physics* 14, no. 7 (2012): 2434–2442, https://doi.org/10.1039/c2cp22419d.

25. M. C. Biesinger, B. P. Payne, A. P. Grosvenor, L. W. M. Lau, A. R. Gerson, and R. S. C. Smart, "Resolving Surface Chemical States in XPS Analysis of First Row Transition Metals, Oxides and Hydroxides: Cr, Mn, Fe, Co and Ni," *Applied Surface Science* 257, no. 7 (2011): 2717–2730, https://doi.org/10.1016/j.apsusc.2010.10.051.

26. E. S. Ilton, J. E. Post, P. J. Heaney, F. T. Ling, and S. N. Kerisit, "XPS Determination of Mn Oxidation States in Mn (hydr)oxides," *Applied Surface Science* 366 (2016): 475–485, https://doi.org/10.1016/j.apsusc.2015.12.159.

27. L. Angeletti, M. Agostini, B. A. M. Figueira, et al., "A Sustainable δ-MnO_2 Derived From Amazon Rainforest Mn-ore Tailings for Applications in Lithium-Ion Batteries," *Sustainable Materials and Technologies* 44 (2025): e01347, https://doi.org/10.1016/j.susmat.2025.e01347.

28. N. Bahlawane, P. H. T. Ngamou, V. Vannier, T. Kottke, J. Heberle, and K. Kohse-Höinghaus, "Tailoring the Properties and the Reactivity of the Spinel Cobalt Oxide," *Physical Chemistry Chemical Physics* 11, no. 40 (2009): 9224–9232, https://doi.org/10.1039/b910707j.

29. J. C. Medina, O. Miguel-Lopez, S. E. Rodil, and R. Zanella, "Surface Functionalization of Mesoporous Co_3O_4 and MnOx With Sodium for the Soot Oxidation Reaction," *Topics in Catalysis* 65, no. 7-8 (2022): 766–778, https://doi.org/10.1007/s11244-022-01595-5.

30. S. Bernardini, F. Bellatreccia, A. C. Municchia, G. D. Ventura, and A. Sodo, "Raman Spectra of Natural Manganese Oxides," *Journal of Raman Spectroscopy* 50, no. 6 (2019): 873–888, https://doi.org/10.1002/jrs.5583.

31. C. M. Julien, M. Massot, and C. Poinsignon, "Lattice Vibrations of Manganese Oxides: Part I. Periodic Structures," *Spectrochimica Acta Part A: Molecular and Biomolecular Spectroscopy* 60, no. 3 (2004): 689–700, https://doi.org/10.1016/S1386-1425(03)00279-8.

32. B. Gilbert, B. H. Frazer, A. Belz, et al., "Multiple Scattering Calculations of Bonding and X-Ray Absorption Spectroscopy of Manganese Oxides," *The Journal of Physical Chemistry. A* 107, no. 16 (2003): 2839–2847, https://doi.org/10.1021/jp021493s.

33. Y. Xu, H. Jiang, X. Li, H. Xiao, W. Xiao, and T. Wu, "Synthesis and Characterization of Mn-Based Composite Oxides With Enhanced Electrocatalytic Activity for Oxygen Reduction," *Journal of Materials Chemistry A* 2, no. 33 (2014): 13345–13351, https://doi.org/10.1039/c4ta02544j.

34. A. C. Queiroz and F. H. B. Lima, "Electrocatalytic Activity and Stability of Co and Mn-Based Oxides for the Oxygen Reduction Reaction in Alkaline Electrolyte," *Journal of Electroanalytical Chemistry* 707 (2013): 142–150, https://doi.org/10.1016/j.jelechem.2013.08.039.

35. Y. Xu, F. Zhang, T. Sheng, et al., "Clarifying the Controversial Catalytic Active Sites of Co_3O_4 for the Oxygen Evolution Reaction," *Journal of Materials Chemistry A* 7, no. 40 (2019): 23191–23198, https://doi.org/10.1039/c9ta08379k.

36. Y. Zhao, B. P. Setzler, J. Wang, et al., "An Efficient Direct Ammonia Fuel Cell for Affordable Carbon-Neutral Transportation," *Joule* 3, no. 10 (2019): 2472–2484, https://doi.org/10.1016/j.joule.2019.07.005.

37. X. Sun, B. Ma, J. Hao, et al.," Insight Into Mass and Charge Transports in Alkaline Direct Ammonia Fuel Cell With Anti-Ammonia Poisoning Fe-N-C Cathode," *Appplied Energy* 401 (2025):126727, https://doi.org/10.1016/j.apenergy.2025.126727.

Supporting Information

Additional supporting information can be found online in the Supporting Information section.